A NUMERICAL STUDY ON MIXING OF TRANSVERSE INJECTION IN SUPERSONIC COMBUSTOR

Mohammad Ali, S. Ahmed and A.K.M. Sadrul Islam

Department of Mechanical Engineering, Bangladesh University of Engineering and Technology Dhaka, 1000, Bangladesh, mail@me.buet.ac.bd

(Received: February 3, 2003 – Accepted in Revised Form: December 25, 2003)

Abstract A numerical study on mixing of hydrogen injected transversely into a supersonic air stream has been performed by solving Two-Dimensional full Navier-Stokes equations. An explicit Harten-Yee Non-MUSCL Modified-flux-type TVD scheme has been used to solve the system of equations, and a zero-equation algebraic turbulence model to calculate the eddy viscosity coefficient. The main objectives of this study are to increase the mixing and combustion efficiencies, and the flame holding capability of a supersonic combustor. The performance of combustor has been investigated by varying the distance of injector position from left boundary keeping constant the backward-facing step height and other calculation parameters. The results show that the configuration for small distance of injector position has high mixing efficiency but the upstream recirculation cannot be evolved properly, which is an important factor for flame holding capability. On the other hand, the configuration for very long distance has lower mixing efficiency due to lower gradient of hydrogen mass concentration on the top of injector caused by the expansion of side jet in both upstream and downstream of injector. For moderate distance of injector position, large and elongated upstream recirculation can evolve which might be activated as a good flame holder.

Key Words Scramjet Engine, TVD Scheme, Backward-Facing Step, Mixing, Supersonic Stream, Flame Holding

چکیده با حل عددی معادله دو بعدی کامل نویر استوکس، اختلاط هیدروژن تزریق شده در جهت متقاطع به داخل جریان فوق سرعت صوت هوا بررسی شده است. برای حل دستگاه معادله ها، از شار اصلاح شده TVD Harten-Yee Non-MUSCL و برای محاسبه ضریب لزجت گردابی از معادله صفر مدل تلاطم جبری استفاده شده است. هدف اصلی این تحقیق، افزایش بازدهی اختلاط و احتراق و بالا بردن قابلیت حفظ شعله در یک مشعل سوپر سونیک است. عملکرد مشعل از طریق تغییر فاصله وسیله تزریق از مرز چپ، در شرایط ارتفاع گام برگشت و سایر پارامترها ثابت، تعیین شده است. نتایج نشان می‌دهد که در وضعیتی که فاصله وسیله تزریق کوچک است، بازدهی بالا است؛ اما به علت دشواری جرخش در جهت مخالف جریان، قابلیت حفظ شعله کم است. از طرف دیگر، وقتی فاصله وسیله تزریق خیلی زیاد است، به سبب شیب کم غلظت هیدروژن در بالای مشعل به علت انبساط جت در هر دو جهت موافق و مخالف، بازدهی اختلاط کوچک می‌باشد. در فاصله های متوسط، ناحیه تجدید چرخش بزرگ و کشیده شده و شعله بخوبی حفظ می‌شود.

1. INTRODUCTION

Mixing of fuel with oxidizer and their combustion are encountered in many engineering applications including hypersonic propulsion system in space vehicles. Particularly, the fuel injection method in hypersonic vehicles incorporating Scramjet (Supersonic Combustion Ramjet) engines requires special attention for efficient mixing and stable combustion. The main problem that arises in this regard concerns mixing of reactants, ignition, flame holding, and completion of combustion. In fact, in supersonic combustion, high penetration and mixing of injectant with main stream is difficult due to their short residence time in combustor [1,2]. Perpendicular injection causes rapid mixing of injectant with main stream and is used to some degree at all flight Mach numbers to promote mixing and reaction, particularly in upstream portion of the combustor. We used perpendicular injection due to (i) its extensive use in Scramjet program, and (ii) high Mach number (M = 5) of main flow.

Both experimental and numerical investigations

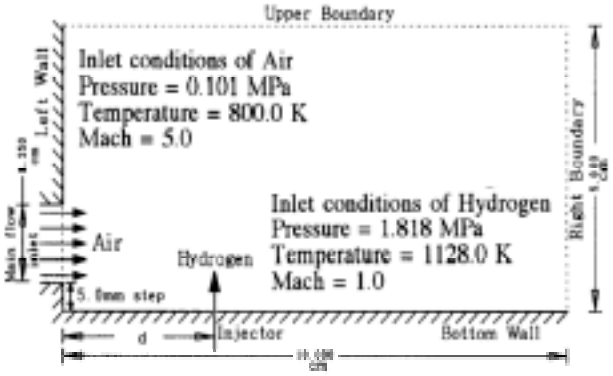

Figure 1. Schematic of physical model. Case 1: d = 10 mm, Case 2: d = 20 mm, Case 3: d = 30 mm, Case 4: d = 40 mm and Case 5: d = 50 mm.

have been performed to analyze the mixing and combustion characteristics, and find out the means of increasing the mixing efficiency. In these investigations the authors showed a number of parameters that can affect the penetration and mixing. In an experiment, Rogers [3] showed the effect of ratio between jet dynamic pressure and freestream dynamic pressure on the penetration and mixing of a sonic hydrogen jet injected normally to an air stream with M = 4. In similar flow arrangements, Kraemer et al. [4] found that the relative change in jet momentum was directly proportional to the relative size between the flow field disturbance and the upstream separation distance.

The downstream injectant penetration height is directly proportional to the upstream separation distance, and, thus, the downstream mixing is dependent on the relative change in jet momentum. Holdeman et al. [5] and Thayer III, et al. [6] derived similar conclusions. Thayer III, et al. [6] also found that the injectant concentration of the separated region was high at all conditions investigated. Heister et al. [7] conducted a calculation on the penetration and bow shock shape of a non-reacting liquid jet injected transversely into a supersonic flow and obtained a correlation between mass loss, boundary layer thickness, recirculation and related parameters. Ali et al. [8,9] studied the mixing mechanisms and investigated mixing and combustion characteristics for several flow configurations. In mixing analysis it was observed that the backward-facing step in finite flow plays an important role in enhancing the mixing and penetration in both upstream and downstream of injector. Investigation proved that without diffusion, although injectant can spread due to species continuity equations, but does not mix with mainstream.

In another study Ali et al. [10] investigated the enhancement of mixing by varying the inlet width of air stream. They found that the flow inlet configuration of a supersonic combustor plays an important role on mixing.

The present investigation has been conducted to see the effect of injector position on mixing and flame holding capability in supersonic combustor. The geometric configuration of the calculation domain and the inlet conditions of main and injecting flows are shown in Figure1. The left boundary consists of a backward-facing step of height 5 mm that was found most efficient in mixing by Ali et al. [11] among the conditions investigated. For this study, the injector position from left boundary, 'd' is varied from 10 mm to 50 mm. The inlet conditions of air are used as Weidner et al. [12] except Mach number. We choose the Mach 5.0 for the main flow as the test program has been conducted over the flight Mach number range [13] from 3.0 to 7.0. The inlet widths of air and side jet are used as Ali et al. [10] which showed good performance on mixing. The grid system consists of 194 nodes in the longitudinal direction and 121 in the transverse direction.

2. MATHEMATICAL MODELING

2.1 Governing Equations The flowfield is governed by the two-dimensional full Navier-Stokes equations with conservation equations of species. Body forces are neglected. For non-reacting flow, these equations can be expressed by

$$\frac{\partial U}{\partial t}+\frac{\partial F}{\partial x}+\frac{\partial G}{\partial y}=\frac{\partial F_v}{\partial x}+\frac{\partial G_v}{\partial y} \quad (1)$$

where

$$U=\begin{pmatrix}\rho\\ \rho u\\ \rho v\\ E\\ \rho_i\end{pmatrix},\ F=\begin{pmatrix}\rho u\\ \rho u^2+p\\ \rho uv\\ (E+p)u\\ \rho_i u\end{pmatrix},\ G=\begin{pmatrix}\rho v\\ \rho uv\\ \rho v^2+p\\ (E+p)v\\ \rho_i v\end{pmatrix},$$

$$F_y=\begin{pmatrix}0\\ \sigma_x\\ \tau_{xy}\\ \sigma_x u+\tau_{xy}v+q_x\\ \dot{m}_{ix}\end{pmatrix},$$

$$F_y=\begin{pmatrix}0\\ \tau_{xy}\\ \sigma_y\\ \tau_{yx}u+\sigma_y v+q_y\\ \dot{m}_{iy}\end{pmatrix}.$$

$$P=\sum_{j=1}^{ns}\rho_j R_j T=\sum_{j=1}^{ns}\rho_j\frac{R}{W_j}T$$

$$E=\sum_{j=1}^{ns}\rho_j C_{pj}T-\sum_{j=1}^{ns}\rho_j\frac{R}{W_j}T+\frac{\rho}{2}\left(u^2+v^2\right)$$

The above terms are expressed as.

$$q_x=\kappa\frac{\partial T}{\partial x}+\rho\sum_{j=1}^{ns}D_j H_j\frac{\partial Y_j}{\partial x},$$

$$q_y=\kappa\frac{\partial T}{\partial y}+\rho\sum_{j=1}^{ns}D_j H_j\frac{\partial Y_j}{\partial y}.$$

$$\dot{m}_{ix}=\rho D_i\frac{\partial Y_i}{\partial x},\quad \dot{m}_{iy}=\rho D_i\frac{\partial Y_i}{\partial y},\quad \lambda=-\frac{2}{3}\mu.$$

The values of C_p and H are considered as functions of temperature and determined from the polynomial curve fitting developed by Moss [14]. Temperature is calculated by Newton-Raphson method.

2.2 Transport Properties The molecular viscosity coefficient μ and thermal conductivity κ of each species are determined by Sutherland formula [15] as

$$\frac{\mu_i}{\mu_0}=\left(\frac{T}{T_0}\right)^{1.5}\frac{T_0+S_l}{T+S_l},$$

$$\frac{\kappa_i}{\kappa_0}=\left(\frac{T}{T_0}\right)^{1.5}\frac{T_0+S_l}{T+S_l} \qquad (2)$$

and those of gas mixture by Wilke's formula [15] and Wassiljewa's equation [16], respectively as

$$\mu_l=\sum_{i=1}^{ns}\frac{z_i\mu_i}{\sum_{j=1}^{ns}z_j\varphi_{ij}},$$

$$\kappa_l=\sum_{i=1}^{ns}\frac{\kappa_i}{1+\frac{1}{z_i}\sum_{\substack{j=1\\ j\neq i}}^{ns-1}A_{ij}z_j} \qquad (3)$$

where

$$\varphi_{ij}=\frac{\left[1.0+(\mu_i/\mu_j)^{0.5}*(M_j/M_i)^{0.25}\right]^2}{(8+8\,M_i/M_j)^{0.5}}$$

$A_{ij}=1.065\ \phi_{ij}$, z_j are the mole fractions, S_l is the Sutherland constant, while $T_0=293$K, and μ_0 and κ_0 are coefficient of viscosity and thermal conductivity of different species at temperature of 293K.

The effective molecular diffusion coefficient for

each species is determined [16] as

$$D_i = \frac{1 - z_i}{\sum_{\substack{j=1 \\ j \neq i}}^{ns-1} z_j / D_{ij}}$$

$$D_{ij} = \frac{0.001858\ T^{1.5} * \left(\frac{M_i + M_j}{M_i * M_j} \right)^{0.5} * 10^{-4}}{p\ \sigma_{ij}^2\ \Omega_D} \quad (4)$$

where

$$\Omega_D = \left(\frac{T}{T_{\varepsilon ij}} \right)^{-0.145} + \left(\frac{T}{T_{\varepsilon ij}} + 0.5 \right)^{-2.0}$$

$$T_{\varepsilon ij} = \left(T_{\varepsilon i} * T_{\varepsilon j} \right)^{0.5}$$

$$\sigma_{ij} = \frac{1}{2} \left(\sigma_i + \sigma_j \right)$$

T = absolute temperature, and p = pressure.

2.3 Turbulence Model A zero-equation algebraic turbulence model developed by Baldwin and Lomax [17] is used to simulate boundary layer separation, recirculation and shock-expansion regions near the injector. The model is patterned with modifications that avoid the necessity for finding the edge of the boundary layer. According to the model the eddy viscosity μ_t is defined as

$$\mu_t = \begin{cases} (\mu_t)_{inner} & y \leq y_{crossover} \\ (\mu_t)_{outer} & y > y_{crossover} \end{cases} \quad (5)$$

where y is the normal distance from the wall and $y_{crossover}$ is the smallest value of y at which the value of viscosity in the outer region becomes less than or equal to the value of viscosity in the inner region.

The viscosity in the inner region is given by

$$(\mu_t)_{inner} = \rho\, l^2\, |\omega| \quad (6)$$

The mixing length in the inner region l is expressed as

$$l = ky \left[1 - \exp(-y^+ / A^+ \right],$$

$$y^+ = \frac{\rho_w\ u_\tau\ y}{\mu_w} = \frac{\sqrt{\rho_w\ \tau_w}\ y}{\mu_w}, \quad u_\tau = \sqrt{\frac{\tau_w}{\rho_w}} \quad (7)$$

For two-dimensional flow, the magnitude of the vorticity is given by

$$|\omega| = \sqrt{\left(\frac{\partial u}{\partial y} - \frac{\partial v}{\partial x} \right)^2} \quad (8)$$

For the outer region,

$$(\mu_t)_{outer} = K\, C_{CP}\, \rho\, F_{WAKE}\, F_{KLEB}(y) \quad (9)$$

where K is the Clauser constant, C_{CP} an additional constant, and

$$F_{WAKE} = \min\left\{ (y_{max} F_{max}), \left(C_{wk} y_{max} U_{dif}^2 / F_{max} \right) \right\} \quad (10)$$

Here F_{max} is the maximum value of the function

$$F(y) = y|\omega| \left[1 - \exp(-y^+ / A^+) \right] \quad (11)$$

at each y station in the flow domain, and y_{max} is the y coordinate at which this maximum occurs. The function $F_{KLEB}(y)$ is the Klebanoff intermittency factor given by [17]

$$F_{KLEB}(y) = \left[1 + 5.5 \left(\frac{C_{KLEB}\ y}{y_{max}} \right)^6 \right]^{-1} \quad (12)$$

U_{dif} is the difference between the magnitude of the maximum and minimum total velocity in the profile at a fixed *x* station, expressed as

$$U_{dif} = \left(\sqrt{u^2+v^2}\right)_{max} - \left(\sqrt{u^2+v^2}\right)_{min} \qquad (13)$$

where $\left(\sqrt{u^2+v^2}\right)$ is taken to be zero along all x station.

The outer formulation (Equations. 9 and 10) can be used in wakes as well as in attached and $y_{max}F_{max}$ replaces $\delta^* u_e$ in the Clause formulation and the combination separated boundary layer. The product $y_{max}U_{dif}^2/F_{max}$ replaces δU_{dif} in a wake formulation. In effect, the distribution of vorticity is used to determine length scales so that the necessity for finding the outer edge of the boundary layer is removed.

The following constants used for this model are taken from Baldwin and Lomax [17]:

$A^+ = 26, \quad C_{CP} = 1.6, \quad C_{KLEB} = 0.3$

$C_{wk} = 0.25, \quad k = 0.4, \quad K = 0.0168$

The values of the turbulent thermal conductivity of the mixture κ_t and turbulent diffusion coefficient of i-th species D_{it} are obtained from eddy viscosity coefficient μ_t by assuming a constant turbulent Prandtl and Lewis number equal to 0.91 and 1.0, respectively. They can be expressed as

$$\frac{\mu_t C_P}{K_t} = 0.91 \qquad (14)$$

$$\frac{\rho D_{it} C_P}{K_t} = 1.0 \qquad (15)$$

The final values of μ, κ and D_{im} used in the governing equations are

$$\mu = \mu_l + \mu_t \qquad (16)$$

$$\kappa = \kappa_l + \kappa_t \qquad (17)$$

$$D_{im} = D_{iml} + D_{it} \qquad (18)$$

2.4 Numerical Scheme The system of governing equations for non-reacting flow is solved using an explicit Harten-Yee Non-MUSCL Modified-flux-type TVD scheme [18]. The two-dimensional, rectangular physical domain (x, y) is transformed into the computational domain (ξ, η) in order to solve the problem on uniform grids. After applying the transformation, Equation (1) can be expressed as

$$\frac{\partial \hat{W}}{\partial t} + \frac{\partial \hat{F}}{\partial \xi} + \frac{\partial \hat{G}}{\partial \eta} = \frac{\partial \hat{F}_v}{\partial \xi} + \frac{\partial \hat{G}_v}{\partial \eta} \qquad (19)$$

where

$$\hat{W} = J^{-1}W, \quad \hat{F} = J^{-1}(\xi_x F + \xi_y G)$$

$$\hat{G} = J^{-1}(\eta_x F + \eta_y G)$$

$$\hat{F}_v = J^{-1}(\xi_x F_v + \xi_y G_v).$$

$$\hat{F}_v = J^{-1}(\xi_x F_v + \xi_y G_v)$$

The velocities in ξ and η directions are denoted by U and V known as cotravariant velocities and can be expressed as $U = \xi_x u + \xi_y v$, $V = \eta_x u + \eta_y v$. The grid Jacobian J and metric terms are

$$J^{-1} = x_\xi y_\eta - x_\eta y_\xi \ , \quad \xi_x = J y_\eta, \quad \xi_y = -J x_\eta,$$

$$\eta_x = -J y_\xi, \quad \eta_y = J x_\xi \ .$$

For the left hand side of Equation 19, the explicit Non-MUSCL TVD scheme can be written as

$$\hat{W}_{i,j}^{n+1} = \hat{W}_{i,j}^{n} - J_{i,j}\frac{\Delta t}{\Delta \xi}\left(\hat{F}_{i+1/2,j}^{n} - \hat{F}_{i-1/2,j}^{n}\right) -$$

$$J_{i,j}\frac{\Delta t}{\Delta \eta}\left(\hat{G}_{i,j+1/2}^{n} - \hat{G}_{i,j-1/2}^{n}\right) \qquad (20)$$

The variables $\hat{F}$ and $\hat{G}$ can be described as

$$\hat{F}^{n}_{i+1/2,j} = \frac{1}{2}\left(\hat{F}^{n}_{i,j} + \hat{F}^{n}_{i+1,j} + \hat{R}_{i+1/2}\ \hat{\Phi}_{i+1/2} \right) \qquad (21)$$

where $\hat{R}_{i+1/2}$ is an eigen vector matrix and $\hat{\Phi}_{i+1/2}$ is a vector.

2.5 Second-Order TVD Scheme The elements of the vector $\hat{\Phi}_{i+1/2}$ for a second-order TVD scheme, originally developed by Harten and later modified and generalized by Yee [19], are

$$\hat{\Phi}_{i+1/2} = \left\{ \hat{\Phi}^{l}{}_{i+1/2} \right\} =$$

$$\left\{ \sigma\left(\hat{a}^{l}{}_{i+1/2} \right)\left(\hat{g}^{l}{}_{i+1} + \hat{g}^{l}{}_{i} \right) - \psi\left(\hat{a}^{l}{}_{i+1/2} + \hat{\gamma}^{l}{}_{i+1/2} \right)\hat{\alpha}^{l}{}_{i+1/2} \right\}$$

$$l = 1 \sim 5 \qquad (22)$$

$$\sigma(z) = \frac{1}{2}\left\{ \psi(z) - \frac{\Delta t}{\Delta \xi} z^2 \right\} \qquad (23)$$

$$\psi(z) = \begin{cases} z & ; \ |z| \geq \delta_l \\ (z^2 + \delta_l^2)/2\delta_l & ; \ |z| < \delta_l \end{cases} \qquad (24)$$

δ_l is a function that defines the range of entropy correction, and should be a function of the contravariant velocity and the corresponding sound speed for the computations. The form of the function used here is

$$\delta_l = \bar{\delta}\left(|U| + |V| + c\sqrt{\xi_x^2 + \xi_y^2 + \eta_x^2 + \eta_y^2} \right) \qquad (25)$$

with a constant $\bar{\delta}$ set to 0.15. More details about the scheme can be found in Yee [20]. The function $\gamma^{l}_{j+\frac{1}{2}}$ can be defined as

$$\gamma^{l}_{j+\frac{1}{2}} = \sigma\left(\alpha^{l}_{j+\frac{1}{2}} \right) \begin{cases} \left(g^{l}_{j+1} - g^{l}_{j} \right)/\alpha^{l}_{j+\frac{1}{2}} & \alpha^{l}_{j+\frac{1}{2}} \neq 0 \\ 0 & \alpha^{l}_{j+\frac{1}{2}} = 0 \end{cases} \qquad (26)$$

The minmod limiter, simplified form of which can be found in Yee [20], was used to avoid the numerical oscillations at the discontinuity. Examples of the 'limiter` function g^{l}_{j} can be expressed as

$$g^{l}_{j} = \text{minmod}\left(\alpha^{l}_{j-\frac{1}{2}}, \alpha^{l}_{j+\frac{1}{2}} \right),$$

$$g^{l}_{j} = \left(\alpha^{l}_{j+\frac{1}{2}}\ \alpha^{l}_{j-\frac{1}{2}} + \left| \alpha^{l}_{j-\frac{1}{2}}\ \alpha^{l}_{j-\frac{1}{2}} \right| \right) \Big/ \left(\alpha^{l}_{j+\frac{1}{2}} + \alpha^{l}_{j-\frac{1}{2}} \right)$$

$$g^{l}_{j} = \left\{ \alpha^{l}_{j-\frac{1}{2}} \left[\left(\alpha^{l}_{j+\frac{1}{2}} \right)^2 + \delta_2 \right] + \alpha^{l}_{j+\frac{1}{2}} \left[\left(\alpha^{l}_{j-\frac{1}{2}} \right)^2 + \delta_2 \right] \right\} /$$

$$\left[\left(\alpha^{l}_{j+\frac{1}{2}} \right)^2 + \left(\alpha^{l}_{j-\frac{1}{2}} \right)^2 + 2\delta_2 \right],$$

$$g^{l}_{j} = S.\max$$

$$\left\{ 0, \min\left(2\left| \alpha^{l}_{j+\frac{1}{2}} \right|, S.\alpha^{l}_{j-\frac{1}{2}} \right), \min\left(\left| \alpha^{l}_{j+\frac{1}{2}} \right|, 2S.\alpha^{l}_{j-\frac{1}{2}} \right) \right\}$$

$$S = \text{sgn}\left(\alpha^{l}_{j+\frac{1}{2}} \right)$$

Among the various approximate Riemann solvers discussed by Yee [20], we used the Roe's average which is the most common one due to its simplicity and ability to return to the exact solution whenever the variables lie on a shock or contact discontinuity. The time step for calculation is determined by

$$\Delta t = \frac{\text{CFL}}{\max\left\{ |U| + |V| + c(\xi_x^2 + \xi_y^2)^{1/2} + c(\eta_x^2 + \eta_y^2)^{1/2} \right\}} \qquad (27)$$

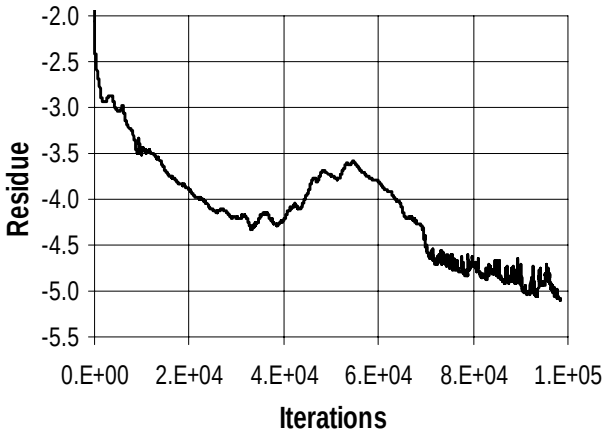

Figure. **2** Convergence history of a typical calculation.

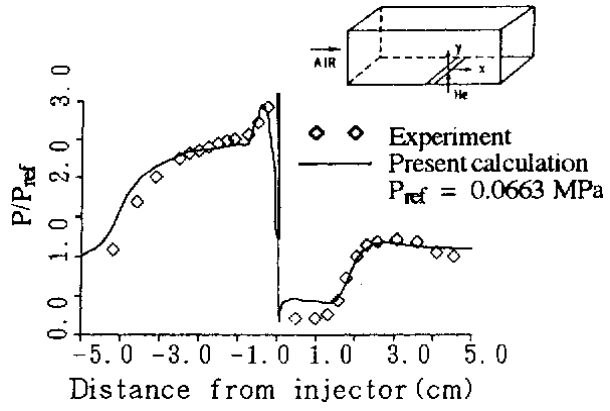

Figure 3. Comparison of experimental and computed pressures along bottom wall.

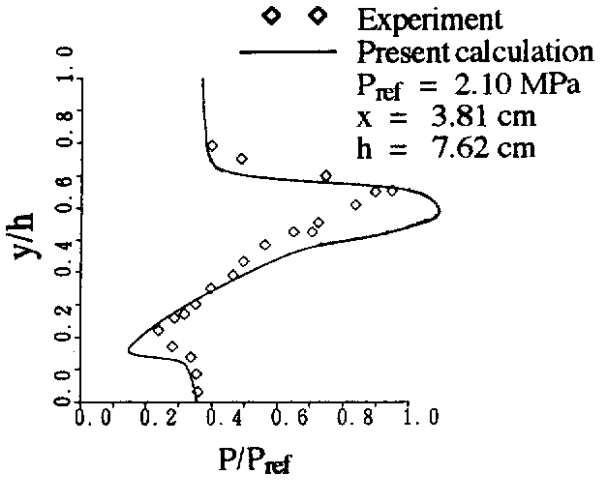

Figure. 4 Comparison of experimental and computed static pressures at 3.81 cm downstream of injector.

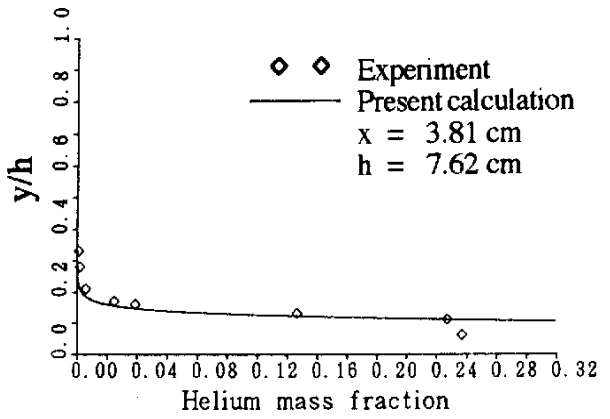

Figure 5. Comparison among helium mass fraction at 3.81 cm downstream of injector.

The CFL is chosen as 0.7 to obtain rapid convergence and avoid unsteadiness in calculation.

3. BOUNDARY CONDITIONS AND CONVERGENCE CRITERION

At wall we set U = 0, V = 0 and $(\partial T/\partial n)_w = 0$. For non-catalytic walls, the normal derivative of species mass fraction also vanishes, and consequently the gradient of total density becomes zero. The pressure is determined from the equation of state. The temperature, pressure, density, and velocity at inflow boundary including the injection are given fixed values. A zero gradient for all variables is used at the outflow boundary. The following convergence criterion has been used:

$$\sqrt{\frac{\sum_{J=1,K=1}^{JJ,KK}\left(\frac{\rho_{new}-\rho_{old}}{\rho_{old}}\right)^2}{JJ.KK}} \le 10^{-5},$$

where JJ and KK are the maximum number of nodes along horizontal and vertical directions,

respectively. A sample convergence history of a typical calculation is shown in Figure 2.

4. NUMERICAL RESULTS

To verify the present code, a comparison has been made with the experimental data published by Weidner et al. [12]. The geometry of the experiment is shown in Figure 3, where helium was injected at sonic condition from a 0.0559 cm slot into a rectangular duct of 25.4 cm long and 7.62 cm high. The slot was located 17.8 cm downstream of the duct entrance. The flow conditions of helium at the slot exit were P = 1.24 MPa, T = 217.0 K and M = 1.0. At the duct entrance, the air stream conditions were P = 0.0663 MPa, T = 108.0 K and M = 2.9. Using the same geometry and flow conditions we computed the flow field with a grid consisting of 246 x 165 nodes along the horizontal and vertical directions, respectively. At the exit of the injector 10 nodal points are used.

Results are given in Figures. 3-5. Figure 3 shows the computed pressure field. This figure shows a pressure rise in the upstream separated region and downstream reattachment region. An over-prediction can be found at the immediate downstream of the injector where the turbulence is naturally intensified by the disturbance caused by the injector. Figure 4 gives the static pressure distribution along the vertical axis at 3.81 cm downstream of the injector. Small variation on the position of recompression shock and bow shock, and the pressures at these positions is observed. In the experiment, the recompression shock occurs at y/h = 0.2 (h is the height of domain), whereas in computation at 0.16. After recompression, both show a linear increase of pressure. The calculation determines the similar difference in the position of bow shock as that of recompression shock. In experiment the position of bow shock is at y/h = 0.63, while in computation it is 0.59. Figure 5 shows the comparison between the mass fraction profiles of injected helium along the same vertical axis at 3.81 cm downstream of the injector. A good agreement does exist in this case. However, the computation shows that the overall results agree with the experiment in spite of the complexities of

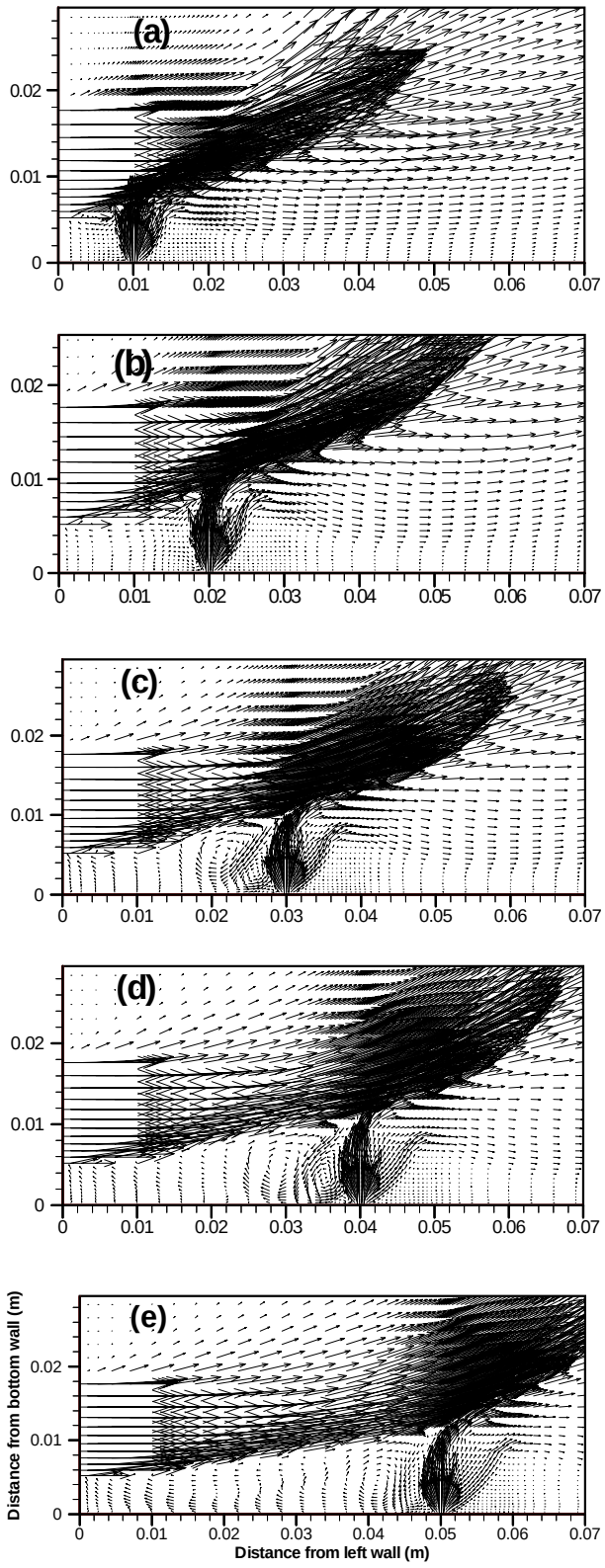

Figurer 6. Velocity vector near injector; (a) Case 1, (b) Case 2, (c) Case 3, (d) Case 4 and (e) Case5.

injected flow field.

Figures 6(a-e) shows the velocity vectors in both upstream and downstream of injector. Strong interaction is occurring between the main and injecting flows in Case 1 shown in Figure 6(a). Due to small space in upstream, two very small recirculations (one is primary and the other is secondary) exist. With the increase of injector distance the recirculation are increasing in areas and the primary one expands towards the left though the pattern of expansion is different. In downstream two features are to be mentioned; (i) no strong recirculation exists in any case, and (ii) for small distance of injector, the injecting jet is bent sharply into downward direction caused by strong interaction of main flow. Another observation is that with the increase in distance of injector position, the expansion of injecting jet plume increases. This is caused by the loss of strength of main flow and early separation of boundary layer.

Figures 7a-e show the penetration and mass concentration of hydrogen. In this paper the term "penetration" is referred to the edge of mixing region in the vertical direction where the mole fraction of hydrogen is 5%. Accordingly the Figure 7 shows that there is little difference in penetration at both upstream and downstream of the configurations. Two competing phenomena are activated in this regard; (i) due to strong interaction in small distance of injector, high gradient of hydrogen mass concentration exists causing high penetration of hydrogen, and (ii) in longer distance of injector, large and elongated upstream recirculation causes high penetration dominated by convection of recirculation. For small distances of injector, most of the upstream region contains high concentration of hydrogen. It can be pointed out that the flame holding requires longer residence time of flame in the burning range and this residence time strongly depends on the geometric expansion of the recirculation zone [21]. The Cases having injector distance d = 20 and 30 mm can produce larger and elongated upstream recirculation where most of the region contains good proportion of hydrogen and oxygen (mole fraction is about 0.4~0.7) exists. Again in cases having d = 40 and 50 mm, far upstream (d = 0~17.5 mm) contains lower mass concentration of hydrogen which is not good for flame holding. In

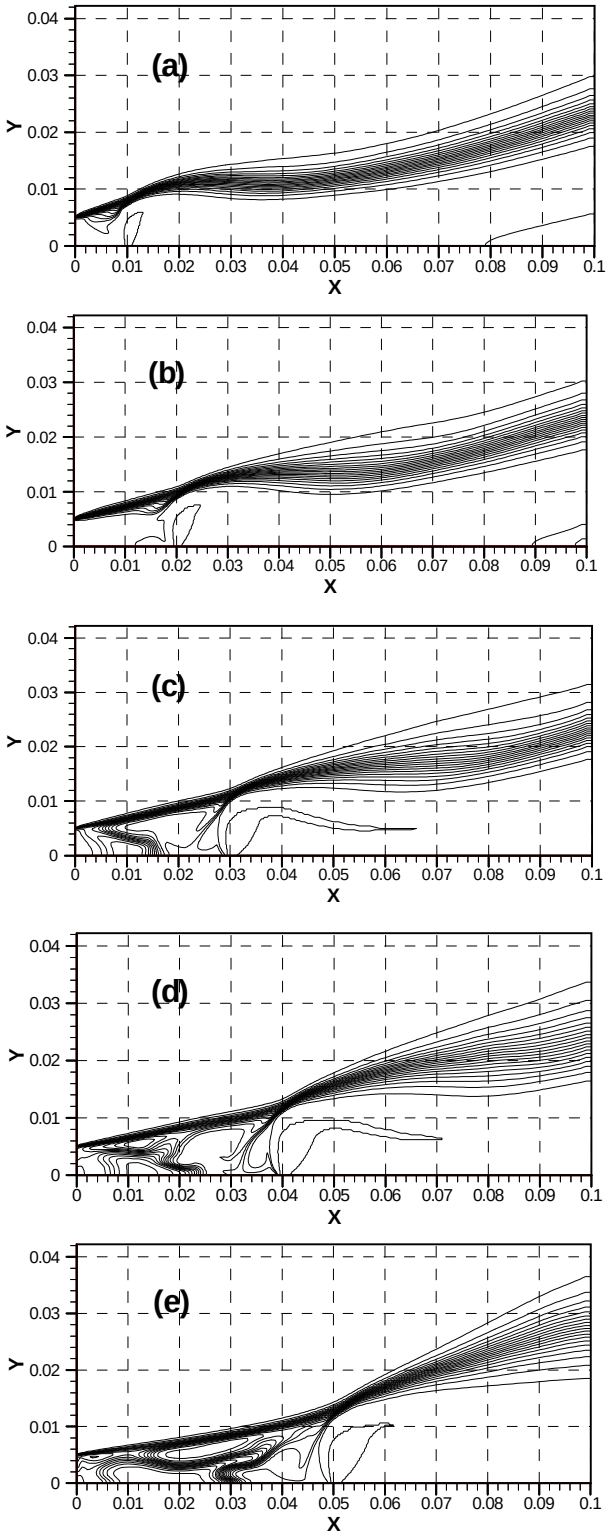

Figure 7. Mole fraction contour of Hydrogen, ϕ (0.05,1.0, 0.05); ϕ is contour level: (a) Case 1, (b) Case 2, (c) Case 3, (d) Case 4, (e) Case 5, X = Horizontal distance (m) and Y = Vertical distance (m).

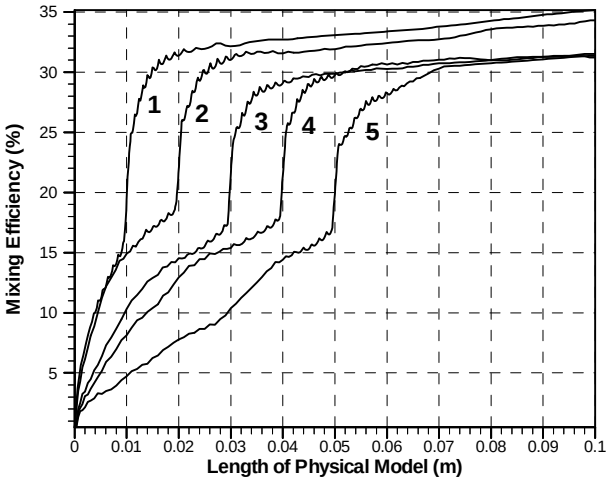

Figure 8. Mixing efficiency along the length of physical model.

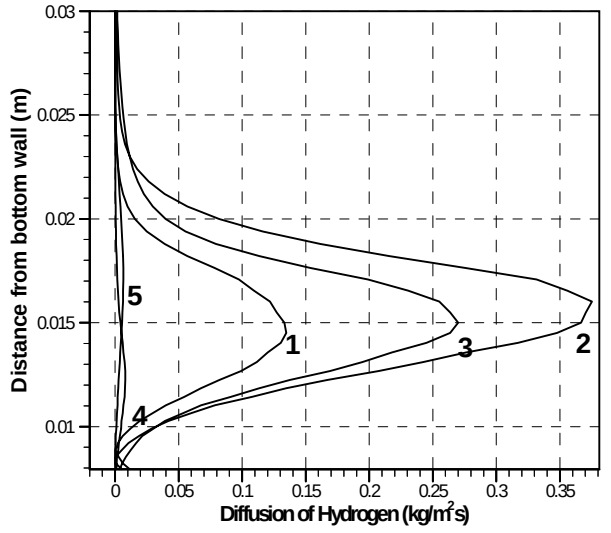

Figure 9. Diffusion of Hydrogen at 0.08 m from left wall.

far downstream the hydrogen distribution is seemed to be better (more uniform) in Cases 3 ~ 5 than that in Cases 1 ~ 2. This uniform distribution of hydrogen is caused by higher expansion of side jet. However, the uniform distribution does not mean higher mixing efficiency, which will be discussed later.

The performance of different cases is evaluated by calculating mixing efficiency. Figure 8 shows the comparison of mixing efficiencies along the length of physical model among different Cases. Mathematically, the mixing efficiency is defined by,

$$\eta_m = \frac{\int_A \left(f_H \ \rho \vec{u} \ d\vec{A} \right) / \phi'}{\dot{m}_H / \Phi}$$

where,

A = arbitrary section plane

f_H = local mass fraction of hydrogen

ρ = total density

$\vec{u}$ = velocity vector

$d\vec{A}$ = small area normal to velocity vector

$\dot{m}_H$ = total mass flux of hydrogen

ϕ' = local equivalence ratio = $\begin{cases} 0.25 & \phi' < 0.25 \\ \phi' & \phi' \geq 0.25 \end{cases}$

Φ = global equivalence ratio = $\begin{cases} 0.25 & \Phi < 0.25 \\ \Phi & \Phi \geq 0.25 \end{cases}$

Φ = global equivalence ratio = 2.0 (for all cases).

Figure 8 shows that the mixing efficiency increases sharply at injector position of different cases. The upstream region shows higher increase of mixing than that of downstream. Due to small distance of injector from left wall, Case 1 has strong interaction between main and injecting flows causing higher mixing efficiency along the length of physical model. In both upstream and downstream, almost same increment of mixing efficiency can be found in Cases 3-5. This trend of efficiency curve indicates that the longer distance of injector position other than Case 2 might increase the cost for construction of combustor. The mixing efficiency of Case 2 is higher than that of Cases 3-5 on the top of injector. In downstream, the increment of mixing is slower for all cases caused by the supersonic nature of flow. However, among the cases investigated, Case 2 has the maximum increasing rate of mixing in downstream. This increasing rate of mixing can be understood by Figure 9, which shows the diffusion

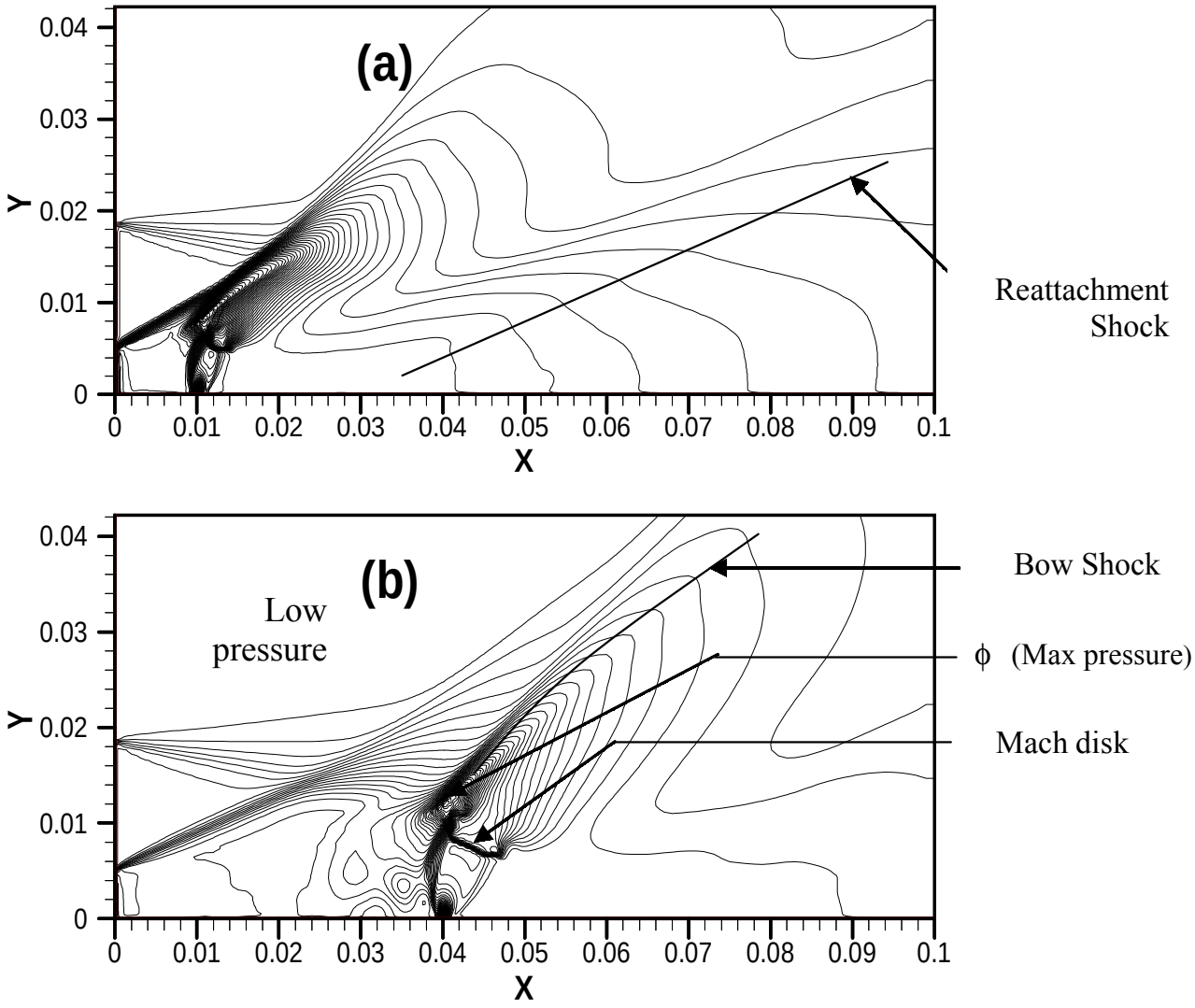

Figure 10. Pressure distribution at 0.08 m from left wall.

of hydrogen along the vertical axis at a distance 80 mm from left wall. From this figure we see that Case 2 has the maximum hydrogen diffusion, which indicates higher, mixing rate in downstream. With the increase of injector distance from d = 10-20 mm, diffusion increases and then decreases for further increase of d. This is quite expected, because for small value of d, the pressure in downstream increases due to earlier reattachment shock which eventually causes the decrease of diffusion. On the other hand, for higher value of d, the injecting jet plume expands more which causes lower mass concentration of hydrogen and eventually diffusion decreases.

Characteristics phenomena such as separation shock, bow shock, Mach disk and reattachment shock can be seen in Figures 10 and 11. Figure 10 shows the pressure contours of only Cases 1 and 4 by which the pressure distribution and different shocks can be understood. Flow separation is

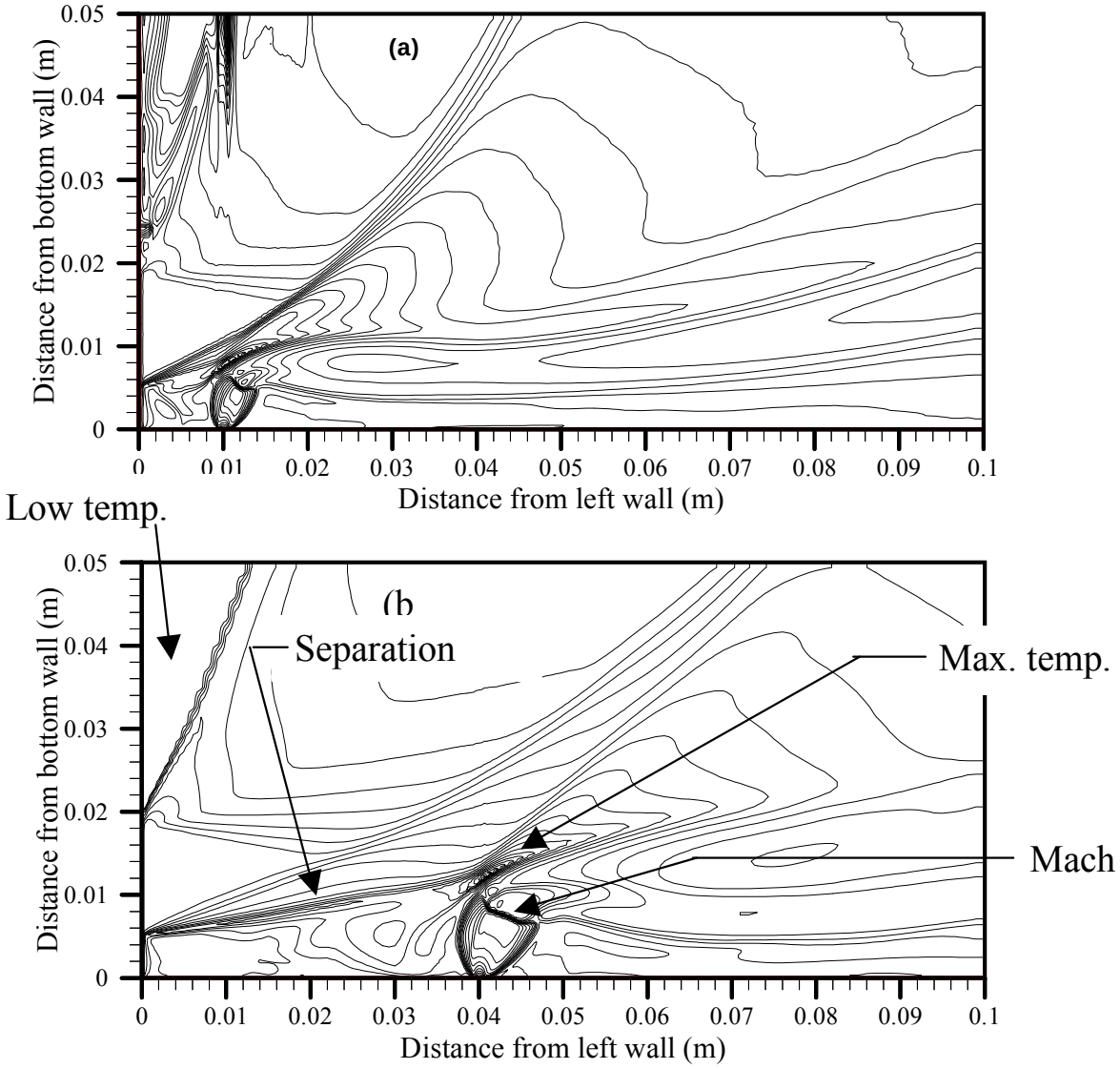

Figure 11. Temperature contour (a) Case 1 and (b) Case 4.

initiated by the backward-facing step at left boundary. The main flow is deflected upward by the existence of wall at the upper part of the left boundary. The deflection angle decreases with the increase of injector distance caused by weak interaction. The under expanded side jet rapidly expands and forms a Mach disk and a bow shock due to the interaction with main flow.

The Maximum pressure in the flow field raises about 2.3×10^6 Pa immediately behind the intersection of separation shock. In the downstream region the reattachment shock is more visible in the pressure contour of Figure 10. Figure 11 shows the temperature distribution in the flow fields. The different shocks and interactions can also be understood from this figure. The maximum temperature of the flow field is about 2280 K occurred near the interaction of separation shock and bow shock.

The top-left corner of the flow field is cold region where the temperature is about 250 K. In case 1, more deflection of main flow to upward direction can be found caused by the early interaction of side jet.

5. CONCLUSIONS

The small distance of the injector position increases the mixing efficiency but decreases the flame holding capability. The configuration increases the pressure loss with the increase of injector distance, which is an important factor for propulsion system. In conclusion, the preferable range of injector position is from 20 ~ 30 mm, more specifically near 20 mm, by which the configuration might act as a good flame holder and become efficient in mixing. For very long distance of injector position (40 mm or more), the configuration reduces both the mixing efficiency and flame holding capability.

6. NOMENCLATURE

c	sound speed	m/s
C_p	specific heat at constant pressure	J/(kg.K)
d	injector distance	mm
D_t	turbulent diffusion coefficient	m^2/s
D_{ij}	binary-diffusion coefficient for species i and j	m^2/s
E	total energy	J/m^3
F	flux vector in x-direction	
$\hat{F}$	transformed flux vector in ξ-direction	
G	flux vector in y-direction	
$\hat{G}$	transformed flux vector in η-direction	
H	enthalpy	J/kg
J	transformation Jacobian	
m	mass flux of species	kg/s
p	pressure	Pa
q	energy flux by conduction	W/m^2
R	universal gas constant	$\frac{J}{kg.mol.K}$
S_l	Sutherland constant for transport coefficients	K
T	temperature	K
T_ε	effective temperature	K
t	physical time	second
u	horizontal velocity	m/s
u_e	velocity at the edge of boundary layer	m
W	vector of conservative variables	
$\hat{W}$	transformed vector of conservative variables	
U	contravariant velocity in ξ-direction	
v	vertical velocity	m/s
V	contravariant velocity in η-direction	
M	molecular weight of species	gm/mol
x	horizontal Cartesian coordinate	m
Y	mass fraction of species	
y	vertical Cartesian coordinate	m
z	mole fraction of species	
ξ	transformed coordinate in horizontal direction	
η	transformed coordinate in vertical direction	
ρ	mass density	kg/m^3
σ	normal stress	Pa
τ	shear stress	Pa
μ	coefficient of dynamic viscosity	kg/(m.s)
κ	thermal conductivity	W/(m.K)
Ω_D	diffusion collision integral	
σ	effective collision diameter	$\dot{A}$
δ	boundary layer thickness	m
δ^*	displacement thickness	m
ϕ'	local equivalence ratio of hydrogen and oxygen	
Φ	global equivalence ratio of hydrogen and oxygen	
φ	contour level	

Superscripts

ns	number of species

Subscripts

i,j index for species
l laminar case
m mixture
t index for turbulence
v viscosity term
x horizontal direction
y vertical direction
xy reference plane
0 reference value, stagnation condition

7. REFERENCES

1. Brown, G. L. and Roshko, A., "On Density Effects and Large Structure in Turbulent Mixing Layer", ***J. Fluid Mechanics***, Vol. 64, No. 4, (1974), 575-816.
2. Papamoschou, D. and Roshko, A., "Observation of Supersonic Free Shear Layers", ***AIAA Paper 86-0162***, (1986).
3. Rogers, R. C., "A Study of the Mixing of Hydrogen Injected Normal to a Supersonic Airstream", ***NASA TN D-6114***, (1971).
4. Kraemer, G. O. and Tiwari, S. N., "Interaction of Two-Dimensional Transverse Jet with a Supersonic Mainstream", ***NASA CR 175446***, (1983).
5. Holdeman, J. D. and Walker, R. E., "Mixing of a Row of Jets with a Confined Crossflow:, ***AIAA Journal***, Vol. 5, No. 2, (1977), 243-249.
6. Thayer III, W. J. and Corlett, R. C., "Gas Dynamic and Transport Phenomena in the Two-Dimensional Jet Interaction Flowfield", ***AIAA Journal***, Vol. 10, (1972), 488-493.
7. Heister, S. D., Nguyen, T. T. and Karagozian, A. R., "Modeling of Liquid Jets Injected Transversely into a Supersonic Crossflow", ***AIAA Journal***, Vol. 27, No. 12, (1989), 1727-1734.
8. Ali, M., Fujiwara, T., "Penetration and Mixing of Hydrogen Injected Normal to a 2-Dimensional Parallel Supersonic Flow", ***Trans. Japan Soc. Aero. Space Sci.***, Vol. 40, No. 130, (1997), 248-261.
9. Ali, M., Fujiwara, T. and Leblanc, J. E., "Influence of Main Flow Inlet Configuration on Mixing and Flameholding in Transverse Injection into Supersonic Airstream", ***International Journal of Engineering Science***, Vol. 38, (2000), 1161-1180.
10. Ali, M. and Islam, A. K. M. S., "Effect of Mainflow Inlet Width on Penetration and Mixing of Hydrogen in Scramjet Combustor", ***Proceedings of the Eighth Asian Congress of Fluid Mechanics***, (December 6-10, 1999), Shenzhen, China, 647–650.
11. Ali, M., Fujiwara, T. and Leblanc, J. E., "The Effects of Backward-Facing Step on Mixing and Flameholding in Supersonic Combustor", ***Journal of Energy, Heat and Mass Transfer***, Vol. 23, (2001), 319-338.
12. Weidner, E. H. and Drummond, J. P., "A Parametric Study of Staged Fuel Injector Configurations for Scramjet Applications", ***AIAA Paper 81-11468***, (1981).
13. Rausch, V. L., McClinton, C. R. and Hicks, J. W., "Scramjet Breath New Life into Hypersonics", ***Aerospace America***, (1997), 344-353.
14. Moss, J. N., "Reacting Viscous-Shock-Layer Solutions with Multicomponent Diffusion and Mass Injection", ***NASA TR-411***, (1974).
15. White, F.M., Viscous Fluid Flow, McGraw-Hill, New York, (1974).
16. Reid, R. C. and Sherwood, T. K., "The Properties of Gases and Liquids", Second Edition, McGraw-Hill, New York, (1966), 520-543.
17. Baldwin, B. S. and Lomax, H., "Thin Layer Approximation and Algebraic Model for Separated Turbulent Flows", ***AIAA Paper 78-257***, (1978).
18. Yee, H. C., "A Class of High-Resolution Explicit and Implicit Shock Capturing Methods", ***NASA, TM 101088***, (1989).
19. Yee, H. C., "Linearized Form of Implicit TVD Schemes for Multidimensional Euler and Navier-Stokes Equations", ***Computers and Mathematics with Applications***, Vol. 12A, (1986), 413-432.
20. Yee, H. C., "Upwind and Symmetric Shock-Capturing Schemes", NASA TM 89464, (1990).
21. Tabejamaat, S. J. Y. and Niioka, T., "Numerical Simulation of Secondary Combustion of Hydrogen Injected from Preburner into Supersonic Airflow", ***AIAA Journal***, Vol. 35, No. 9, (1997), 1441-1447**.**